

Technical Communication

A shrunken edge algorithm for contact detection between convex polyhedral blocks



Jie Wang, Shihai Li*, Chun Feng

Institute of Mechanics, Chinese Academy of Sciences, Beijing 100190, China

ARTICLE INFO

Article history:

Received 7 June 2014

Received in revised form 15 October 2014

Accepted 15 October 2014

Available online 7 November 2014

Keywords:

Contact detection

Polyhedral block

Geometric resolution

Contact type

Shrunken edge

Approaching face

ABSTRACT

The detection of contacts between interacting blocks is an important but time-consuming calculation in discontinuity-based numerical methods. This paper presents a new algorithm for the detection of contacts between arbitrary convex polyhedra with planar boundaries. In this algorithm, a pair of contacting blocks is identified as a main block and a target block. The concept of a shrunken edge is introduced in this paper. First, each vertex of the main block is shrunk toward the centre of the neighbouring faces. The shrinkage is infinitesimal yet useful for contact detection. Shrunken edges parallel to the original edges on the main block are established by connecting the shrunken points. Contact detection is then performed by determining the geometric relationship between a shrunken edge and its approaching face on the target block. From the three possible geometric relationships, all six contact types in three dimensions can be identified precisely, which allows for an easy and efficient detection process. Finally, the accuracy and effectiveness of the new contact algorithm are demonstrated through several examples in which two or more blocks collide in a three-dimensional domain.

© 2014 Elsevier Ltd. All rights reserved.

1. Introduction

Geomaterials are typically discontinuous, containing joints and pre-existing cracks, and their failure is typically a combined continuum-discontinuum problem [1–3]. The properties and engineering behaviour of rock masses are typically governed by discontinuities. Thus, conventional numerical methods, which mainly use continuous models, are not suitable for such situations [4].

Methods of computational mechanics of discontinua include discrete element methods (DEM) [5–7], discontinuous deformation analysis (DDA) [8–11], the combined finite-discrete element method (FDEM) [12,13] and the numerical manifold method (NMM) [14,15]. The key to any discontinuity-based numerical method is a rigorous contact theory that can describe the interactions of multiple three-dimensional (3D) blocks [16]. Developing such a theory is a difficult task because contacts may exist between any combination of vertices, edges and faces, and contacts between blocks must be identified and updated continuously throughout the computation process [17]. Contact detection is still a major challenge in large-scale simulation despite advances in computer hardware and parallel techniques.

Contact detection is typically performed in two independent stages. The first stage, called a neighbour search, is a rough search that aims to optimally find the number of possible blocks in contact [18,19]. The most recent algorithms developed for neighbour searching include the no-binary-search algorithm [20], the spatial partitioning algorithm [21], the DESS algorithm [22] and the sweep-and-prune algorithm [23]. In the second stage, called geometric resolution, pairs of potentially contacting blocks obtained in the first stage are examined in detail to identify the contact type and calculate the contact forces. Cundall [5] introduced the well-known class of common plane (CP) methods. By translating and rotating the common plane, the contact type can be determined based on the number of vertices touching the common plane. This method has a complexity of order $O(N)$ and has been successfully implemented in the 3D DEM code 3DEC [24]. Nezami et al. [25] showed that the number of iterations needed to find the correct CP for a contact between two blocks using conventional algorithms depended on the accuracy of the initial guess for the CP. They proposed the fast common plane (FCP) method to obtain the common plane, which was up to 40 times faster than the available search methods. Nezami et al. [26] proposed the shortest link method (SLM) to improve the efficiency in finding the accurate CP of a contact.

The Lin-Canny [27] closest features algorithm is a more sophisticated feature-based algorithm that computes the distance

* Corresponding author.

between disjoint polyhedra. The algorithm tracks and catches the closest features of a pair of convex polyhedral blocks. Mirtich [28] presented the V-Clip collision detection algorithm, which tracked the closest pair of features between convex polyhedra. Wu et al. [29] presented an algorithm that found vertex-to-face contacts as the first step toward a more comprehensive 3D analysis. Yeung et al. [30] and Jiang and Yeung [16] developed a point-to-face model, which formed part of a contact method to be used in 3D DDA. Wu [31] presented a new edge-to-edge contact calculation algorithm in which edge-to-edge contacts were transformed into vertex-to-face contacts. Yeung et al. [32] developed an edge-to-edge contact model that included methods for detecting the contact type and predicting the face where the first entrance would occur, as well as criteria for interpenetration. Contact transformation improved the efficiency of the calculation procedure. Keneti et al. [17] introduced a new algorithm for the detection of all contact types between convex blocks. After one of the approaching faces was identified as the main plane and the vertices within a certain distance were located, different algorithms were used to search for contact points and identify contact types in the global coordinate system. Beyabanaki et al. [33] presented a contact calculation algorithm for contacts between two polyhedra. In this algorithm, contact types were calculated from topological information about the two nearest points of the polyhedra. Boon et al. [34] introduced an algorithm for contact detection between convex polygonal and polyhedral particles in which a set of linear inequalities was used to define the space occupied by a polygon or polyhedron. Feng et al. [35] introduced a semi-spring and semi-edge contact model that could improve the efficiency of contact detection and simplify the steps for calculating contact forces.

The algorithm presented in this paper is intended to be a simple and useful tool for the resolution stage of contact detection. All six contact types can be identified precisely and efficiently by determining the geometric relationship between a shrunken edge and its approaching face. This new algorithm has been implemented in a computer program, and numerical results from several examples are provided to demonstrate the effectiveness of the algorithm.

2. Identification of the contact condition using shrunken edges

In contact search algorithms, the contact type is important because it determines the mechanical response of the contact. There are six types of contact for 3D blocks: vertex-to-vertex, vertex-to-edge, vertex-to-face, edge-to-edge, edge-to-face and face-to-face. The simplest approach is to test all possibilities, but this process is time consuming and unnecessary. In three dimensions, there are internal connecting links between the vertices, edges and faces. These links can be utilised to improve efficiency. In this section, we describe a shrunken edge model for computing the distance to an approaching face on a target block that can detect all six contact types between arbitrary convex polyhedra.

2.1. The concept of a shrunken edge

In hybrid continuous-discontinuous numerical methods, such as FDEM and NMM, blocks are initially neatly stacked, forming a continuous medium. Additionally, vertices and edges are shared by neighbouring faces. In this condition, it is difficult to identify contacts as vertex-to-vertex or edge-to-edge. In some cases, the contact condition cannot be determined correctly. As an example, Fig. 1a shows four blocks (A, B, C and D) with four vertices (a, b, c and d) located at the same position. In vertex-to-vertex contact detection, it is difficult to precisely identify contact between vertex a and vertices b, c and d (Fig. 1b). Similarly, contact detection will

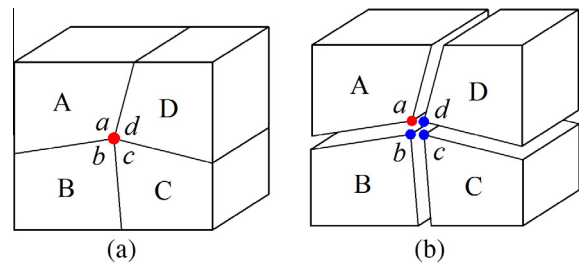


Fig. 1. (a) Vertices located at the same position. (b) Vertex-to-vertex contact is difficult to identify.

be difficult if more than two parallel edges are located together. These conditions are commonly found in hybrid continuous-discontinuous methods; however, few effective solutions have been proposed. To resolve this problem, the shrunken edge model is proposed for contact detection.

A shrunken edge, unlike a conventional edge, is located on a face. It is assumed that each vertex of a block shrinks toward the centre of the neighbouring faces. The shrunken distance is infinitesimal but still useful for contact detection. Then, a shrunken edge parallel to the initial edge is established by connecting the shrunken points. As an example, a hexahedral block is presented in Fig. 2a. V_1 is one vertex of the block, and P_1 is the shrunken point corresponding to V_1 on face α . The position of point P_1 will depend on the shrinkage distance, which can be expressed as

$$|P_1V_1| = \lambda|OV_1| \quad (1)$$

where λ is the shrinkage coefficient, which can be 0.1–1.0% (1.0% is used in this paper). To find the correct contact, the search tolerance should be less than the shrinkage distance. All of the shrunken points in the block are obtained from the vertices in the same manner, and the shrunken edges are established. In Fig. 2b, points P_1 and P_2 are shrunken points and E_1 is a shrunken edge.

Here, the shrunken edge is used only for the geometric resolution phase of contact detection, and the shrinkage coefficient λ can be regarded as a way to set the tolerance for contacts. The initial configuration of the block should be used when calculating the motion and deformation of a block. Therefore, there is no reduction in the block volume in this algorithm.

There are several benefits of the shrunken edge concept. First, it is easier to establish the initial contact conditions in a continuous block system using shrunken edges because the edges used for detection shrink into the neighbouring faces. Furthermore, the seamless transition of a geological body from a continuum to discrete description can be achieved using shrunken edges.

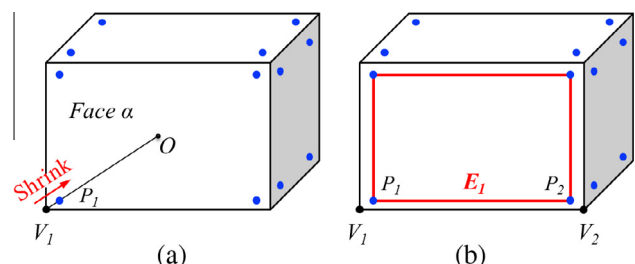


Fig. 2. (a) Shrunken points and (b) shrunken edges of a hexahedral block.

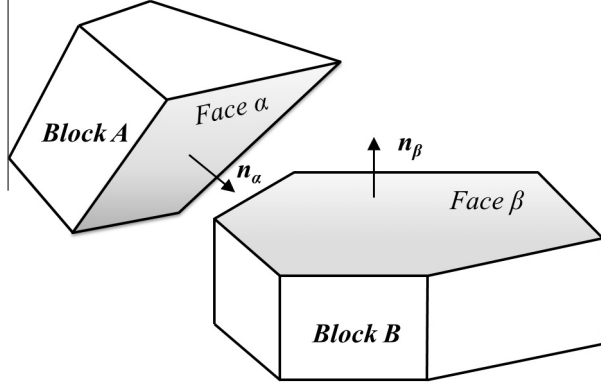


Fig. 3. Approaching faces on two contacting blocks.

2.2. Identification of the contact conditions

In this algorithm, for each pair of contacting blocks, one block is defined as the main block and the other as the target block. Fig. 3 shows two blocks that have possible interactions. Let A be the main block and B be the target block. For efficient computation, contact detection is performed between the approaching faces in blocks A and B. Approaching faces are identified from the angle between their unit normal vectors. The normal vector of a face is perpendicular to the face and points outside the block. As an example, face α lies on main block A, and its unit normal vector is n_α . The face on block B approaching face α can be obtained by determining the minimum value of

$$V_i = \mathbf{n}_\alpha \cdot \mathbf{n}_i \quad (2)$$

where \mathbf{n}_i are the unit normal vectors of the faces on block B. In this manner, for each face on the main block, defined as a main face, an approaching face is found on the target block. Contact detection is then performed between the main face and its approaching face.

Fig. 4 shows a main face α and its approaching face β . Shrunken edge mn lies on face α . Contact points, types and forces can be obtained by determining the geometric relationship between the shrunken edge and the approaching face. Initially, the distances from the two end points of shrunken edge mn to face β can be calculated as

$$d_m = \mathbf{O}m \cdot \mathbf{n}_\beta, d_n = \mathbf{On} \cdot \mathbf{n}_\beta \quad (3)$$

where \mathbf{n}_β is the outer unit normal vector of face β , \mathbf{Om} is a vector from point O to point m and O is an arbitrary point on face β . After this initial calculation, a small positive user-defined tolerance d_{tol} is used for contact detection. Based on the relationships between d_m , d_n and d_{tol} , four possible conditions between the shrunken edge and approaching face can be derived as follows: (A) $|d_m| > d_{tol}$,

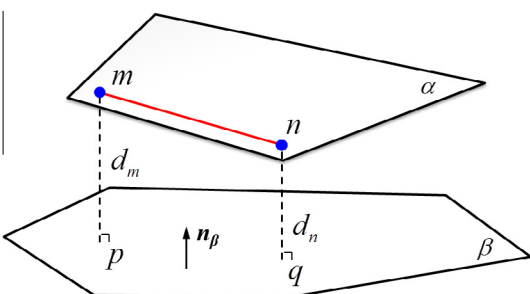


Fig. 4. Contact detection between a shrunken edge and an approaching face.

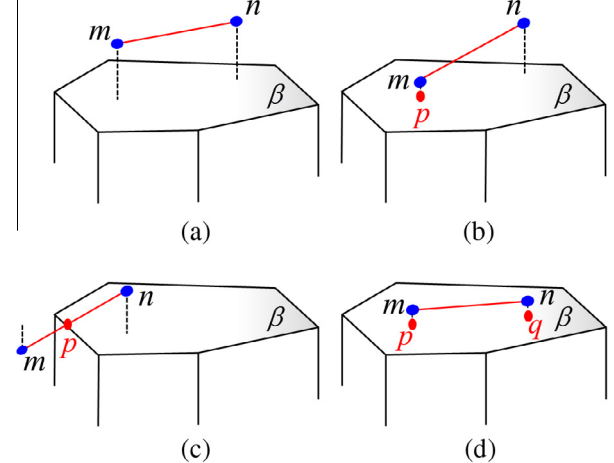


Fig. 5. Possible geometric relationships between a shrunken edge and an approaching face.

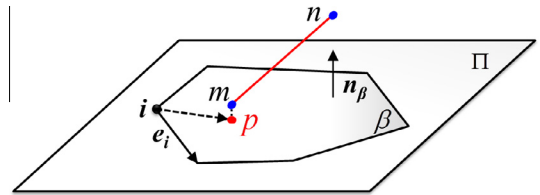


Fig. 6. Illustration of projective point p inside face β .

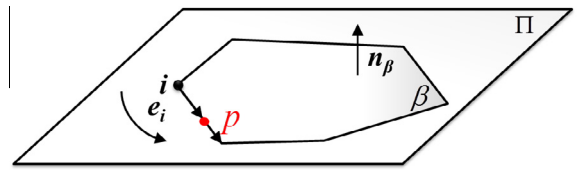


Fig. 7. Illustration of projective point p on an edge of face β .

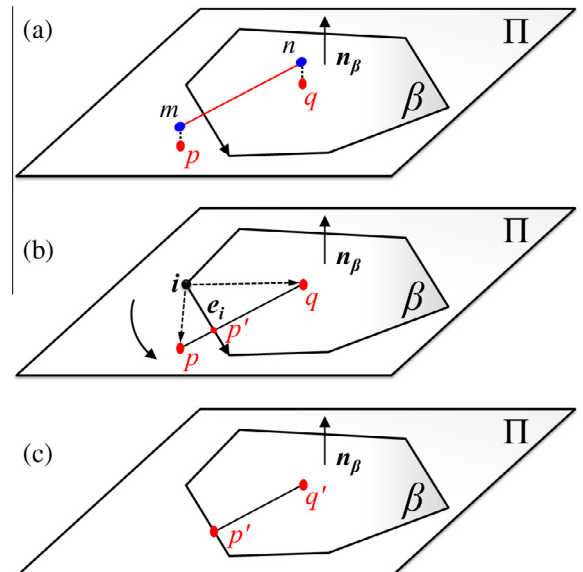


Fig. 8. Illustration of the update process for segment pq on face β : (a) projective points p and q , (b) segment pq cut by edge e_i and (c) updated segment $p'q'$.

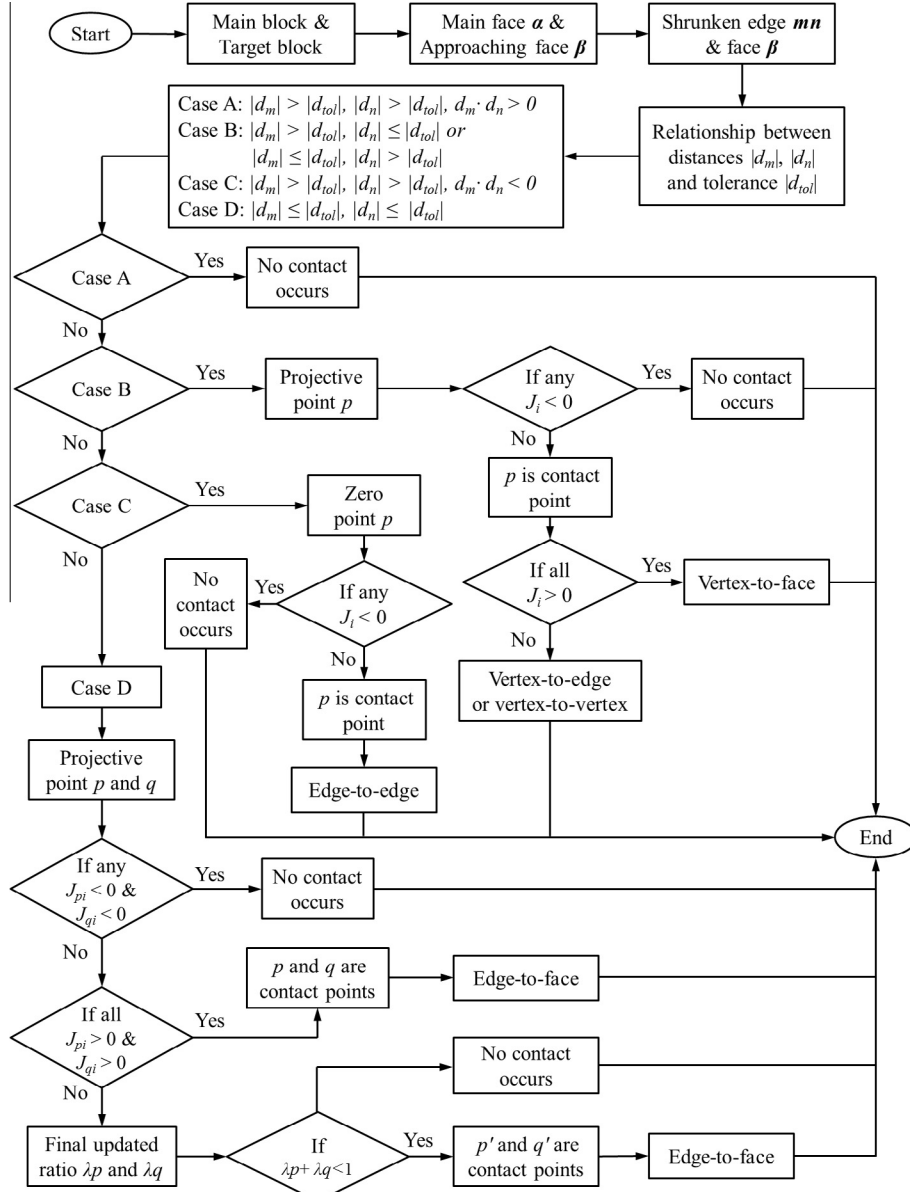


Fig. 9. Algorithm for the detection of contacts between two neighbouring convex blocks.

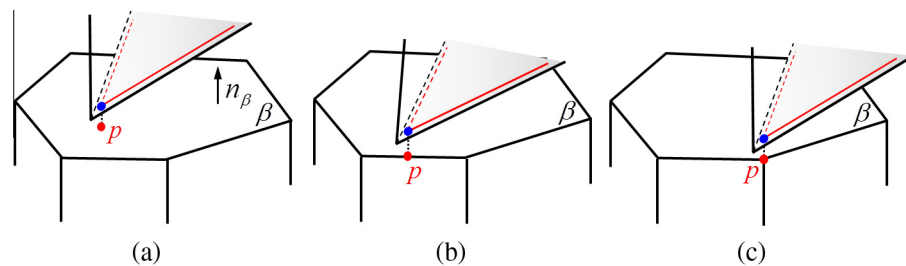


Fig. 10. Contact types in case B: (a) vertex-to-face, (b) vertex-to-edge and (c) vertex-to-vertex.

$|d_n| > d_{tol}$, $d_m \cdot d_n > 0$; (B) $|d_m| > d_{tol}$, $|d_n| < d_{tol}$ or $|d_m| < d_{tol}$, $|d_n| > d_{tol}$; (C) $|d_m| > d_{tol}$, $|d_n| > d_{tol}$, $d_m \cdot d_n < 0$; and (D) $|d_m| < d_{tol}$, $|d_n| < d_{tol}$. These four cases are shown in Fig. 5.

In case A, the absolute values of both d_m and d_n are greater than d_{tol} , and they have the same sign. No contact will occur in this case. Therefore, it is only necessary to analyse the other three cases. For

the analysis, the vertices on face β are numbered in the counter-clockwise direction.

In case B, let Π denote the plane through face β (Fig. 6). If d_m is less than d_{tol} , then let point p be the projection of point m on plane Π . It is necessary to check whether point p is inside face β , which is expressed as

$$J_i = (\mathbf{e}_i \times \mathbf{ip}) \cdot \mathbf{n}_\beta \quad (4)$$

where \mathbf{e}_i ($i = 1 - N$) are the direction vectors of the edges of face β and \mathbf{ip} is the vector from point i to point p . If all values of J_i are greater than zero, then point p is inside the boundary of face β (Fig. 6), and the contact point is p . If point p is outside the boundary of face β , no contact will occur.

In case C, there must be a point p on shrunken edge mn whose distance to plane Π is zero. It is necessary to check whether point p is on any edge of face β . Based on Eq. (4), if any one value of J_i is equal to zero (Fig. 7) and the others are greater than zero, then point p will be on an edge of face β , and the contact point will be p .

In case D, let p and q be the projections of points m and n , respectively, on the approaching plane Π (Fig. 8a). First, it is necessary to check whether segment mn is outside face β . For edge \mathbf{e}_i ($i = 1 - N$) of face β , the values of J_{pi} and J_{qi} can be obtained from Eq. (4). If there is any edge for which both J_{pi} and J_{qi} are less than zero, then segment pq will be outside face β , and no contact will occur. Next, it is necessary to check whether segment mn is inside face β . If the values of J_{pi} and J_{qi} are greater than zero for all edges, then segment pq will be inside face β , and the contact points will be p and q . Finally, if the two conditions above are not satisfied, then a cutting algorithm is performed as follows.

Let λ_p and λ_q denote the length ratios of points p and q , respectively, and let the initial values of both be zero. As shown in Fig. 8b, segment pq is cut by edge \mathbf{e}_i . If point p is outside edge \mathbf{e}_i and q is inside edge \mathbf{e}_i , then the updated length ratio for point p can be calculated as

$$\lambda_{pi} = |\mathbf{pp}'| / |\mathbf{pq}| = \frac{|\mathbf{e}_i \times \mathbf{ip}|}{|\mathbf{e}_i \times \mathbf{ip}| + |\mathbf{e}_i \times \mathbf{iq}|} \quad (5)$$

where \mathbf{e}_i ($i = 1 - N$) are the direction vectors of the edges of face β . After the segment has been cut by all edges, the final length ratio for point p can be obtained from

$$\lambda_p = \min\{\lambda_{pi}\} \quad (6)$$

The final length ratio λ_q for point q can be obtained in the same manner. Based on the two ratios λ_p and λ_q , segment pq is updated, denoted as $p'q'$ (Fig. 8c). The positions of points p' and q' are obtained from

$$\mathbf{pp}' = \lambda_p \mathbf{pq}, \mathbf{qq}' = \lambda_q \mathbf{qp} \quad (7)$$

If the length of segment $p'q'$ is greater than zero, then contact will occur, and the contact points will be p' and q' .

2.3. Corresponding contact types

In the shrunken edge algorithm, there are only three cases (B, C and D) where contact may occur between the shrunken edge and the approaching face. The flowchart of the algorithm for distinguishing the contact types is shown in Fig. 9. The three cases and six contact types in three dimensions (vertex-to-vertex, vertex-to-edge, vertex-to-face, edge-to-edge, edge-to-face and face-to-face) are related. Therefore, contact detection can be performed in practical computer programs by determining which of the three cases applies.

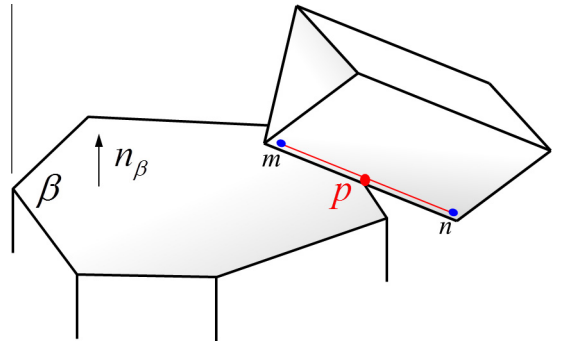


Fig. 11. Edge-to-edge contact in case C.

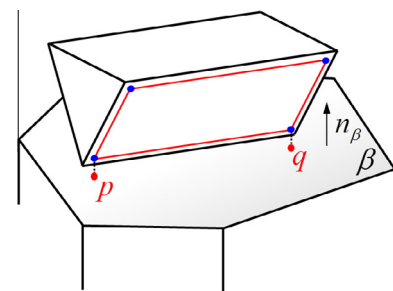


Fig. 12. Edge-to-face contact in case D.

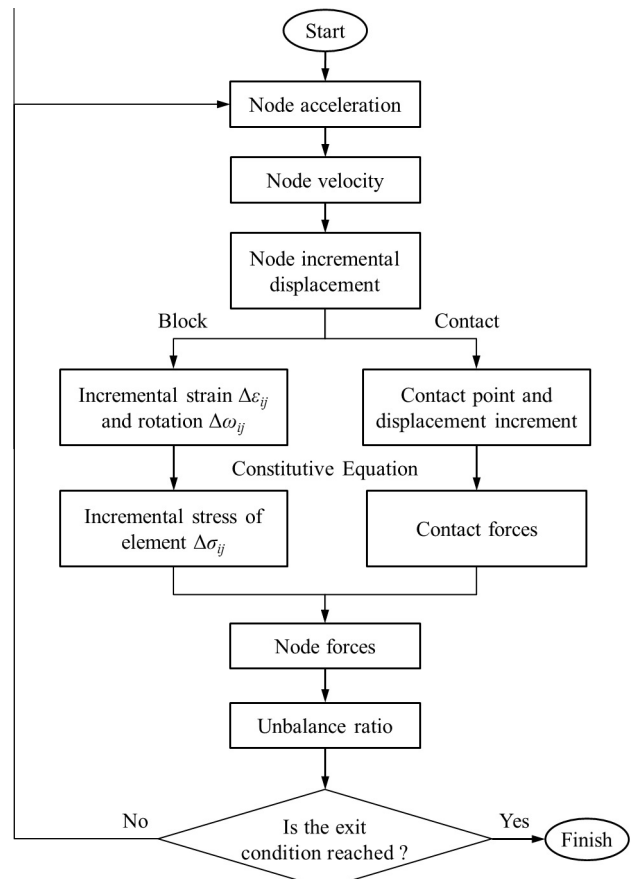


Fig. 13. The use of the deformable discrete element method to solve a geological problem.

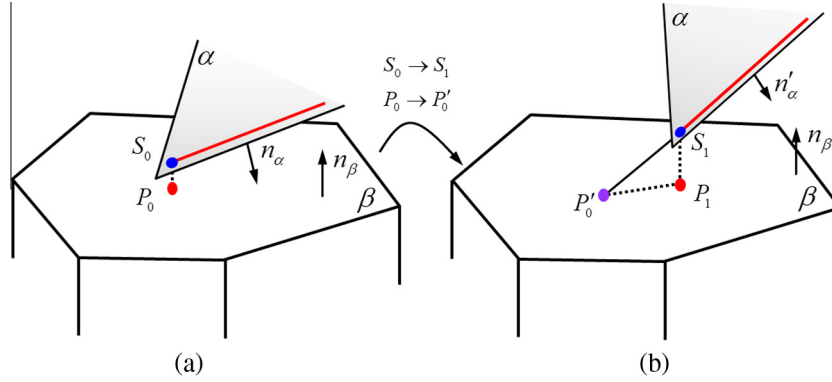


Fig. 14. Position of the shrunken edge and its approaching face: (a) before a displacement increment and (b) after a displacement increment.

In case B (Fig. 5), the possible contact types between the main block and the target block are vertex-to-face, vertex-to-edge and vertex-to-vertex, depending on the position of point p . In vertex-to-face contact, the contact normal is simply the approaching face normal (Fig. 10a). In vertex-to-edge contact, the contact normal is computed by taking the average of the normal vectors of the faces neighbouring the edge (Fig. 10b). In vertex-to-vertex contact, the contact normal is computed by averaging the normal vectors of the faces neighbouring one of the vertices (Fig. 10c).

In case C (Fig. 5), the corresponding contact type is edge-to-edge (Fig. 11). The contact normal is the cross product of the direction vectors of the two edges. For example, the direction vector of edge mn can be obtained from

$$\mathbf{e}_{mn} = \frac{\mathbf{m}\mathbf{n}}{|\mathbf{m}\mathbf{n}|} \quad (8)$$

In case D (Fig. 5), the corresponding contact type is typically edge-to-face (Fig. 12). However, parallel edge-to-edge contact will occur if both points p and q are located on an edge of face β . If more than one edge-to-face contact occurs between faces α and β , then the contact type is face-to-face. In edge-to-face and face-to-face contact, the contact normal is the normal vector of the approaching face on the target block. In parallel edge-to-edge contact, the contact normal can be computed by taking the average of the normal vectors of the faces neighbouring the edge.

3. The deformable discrete element method

Discrete elements were originally introduced to model problems and processes that continuum-based models could not model correctly. However, a large class of problems of discontinua involve individual bodies that can deform, fail, fracture and even fragment [21]. In the deformable discrete element method, each block is discretised into finite elements for deformable analysis. The equations of motion are obtained from the equilibrium conditions of all forces acting on the nodal masses, resulting in a system of equations of the form

$$\mathbf{M}\ddot{\mathbf{u}} + \mathbf{C}\dot{\mathbf{u}} + \mathbf{F}(t) = \mathbf{P}(t) \quad (9)$$

where \mathbf{u} , $\dot{\mathbf{u}}$ and $\ddot{\mathbf{u}}$ denote vectors containing the nodal displacements, velocities and accelerations, respectively; \mathbf{M} is the mass matrix; \mathbf{C} is the damping matrix; and the vectors $\mathbf{F}(t)$ and $\mathbf{P}(t)$ contain the internal and external nodal forces, respectively.

The blocks are discretised into constant-strain tetrahedral finite elements. According to the small deformation hypothesis, the strain increment $\Delta\epsilon_{ij}$ and rotation increment $\Delta\omega_{ij}$ are defined as

$$\Delta\epsilon_{ij} = \frac{1}{2}(\dot{u}_{i,j} + \dot{u}_{j,i})\Delta\tau \quad (10)$$

$$\Delta\omega_{ij} = \frac{1}{2}(\dot{u}_{i,j} - \dot{u}_{j,i})\Delta\tau \quad (11)$$

where $\Delta\tau$ is the calculation time step. The stress increment can be obtained from

$$\Delta\sigma_{ij} = \lambda\Delta\epsilon_{\theta}\delta_{ij} + 2\mu\Delta\epsilon_{ij} \quad (12)$$

in which $\Delta\epsilon_{\theta}$ is the volumetric strain increment, λ and μ are the Lame constants and δ_{ij} is the Kronecker symbol.

When a block rotates, the principal axis of stress will rotate with the element, and the stress components will be changed in

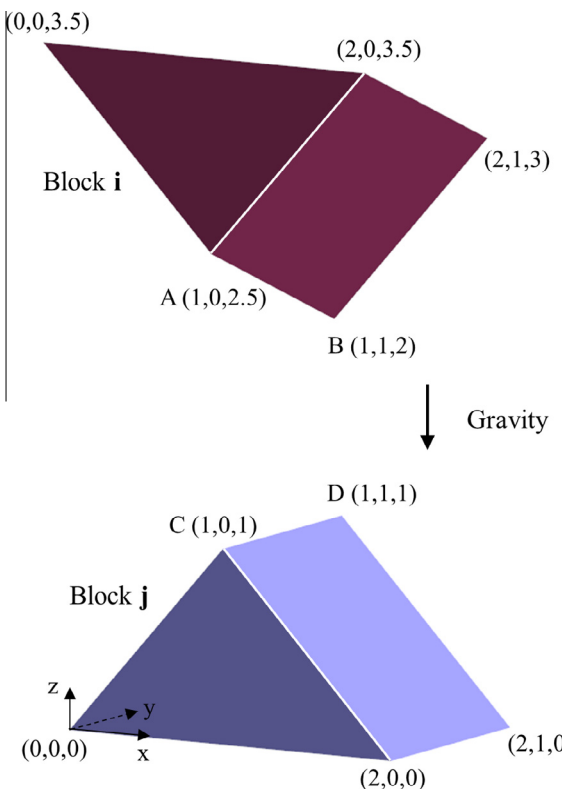


Fig. 15. Initial configuration of a two-block system.

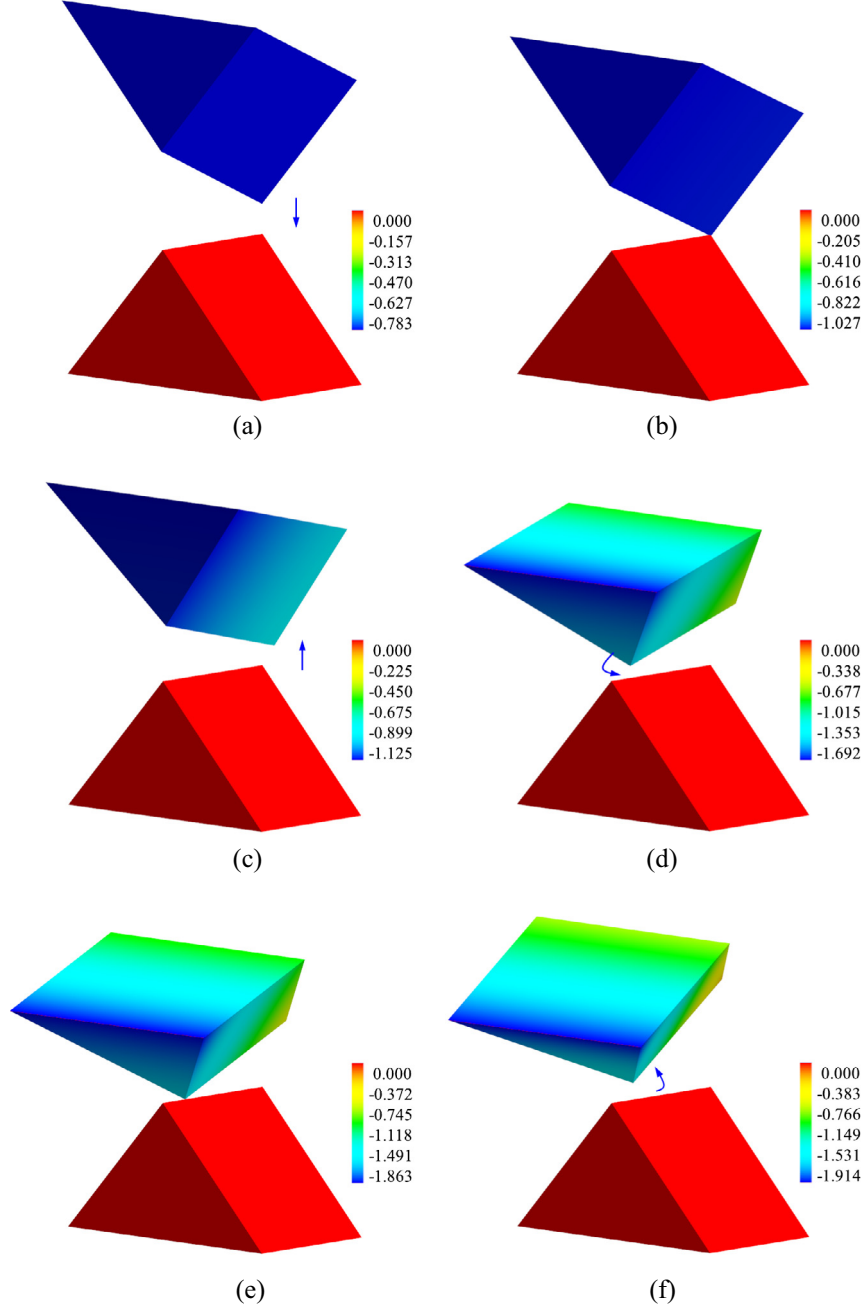


Fig. 16. The displacement in vertical direction of the two-block system after (a) 0.40 s, (b) 0.46 s, (c) 0.52 s (d) 0.72 s, (e) 0.78 s and (f) 0.92 s (unit: m).

the global coordinate system. The revised stress from the preceding step can be calculated from

$$\sigma_{ij}^c(\tau) = \sigma_{ij}(\tau) + \Delta\omega_{ik}\sigma_{kj}(\tau) - \sigma_{ik}(\tau)\Delta\omega_{kj} \quad (13)$$

in which $\sigma_{ij}^c(\tau)$ is the revised stress. The total stress at time $\tau + \Delta\tau$ is

$$\sigma_{ij}(\tau + \Delta\tau) = \sigma_{ij}^c(\tau) + \Delta\sigma_{ij} \quad (14)$$

The nodal force vectors of the tetrahedral elements can be calculated from

$$\{F(\tau + \Delta\tau)\}_i = [B]_i^T [\sigma(\tau + \Delta\tau)]_i w_i J_i \quad (15)$$

where $[B]_i$, $[\sigma]_i$, w_i and J_i are the strain matrix, stress, integral coefficient and Jacobi determinant, respectively, of tetrahedral element i . The nodal force vectors of the block can be obtained by cumulating the nodal forces of all the tetrahedral elements.

Fig. 13 shows the use of the method to solve a typical geological problem. In this figure, the exit condition could be a convergence criterion in a static problem or the calculation time in a dynamic problem. An elastic model is used for the constitutive model of the block in the algorithm. A different constitutive model, for example, to model damage or plasticity, could be used in place of Eq. (12).

4. Calculation of the contact forces

For the three contact possibilities between a shrunken edge and its approaching face, the contact points are obtained as in Section 2.2. In this section, the formulation of the contact forces in the new model is presented, including the normal, shear and frictional forces.

4.1. Normal contact force

In Fig. 14, $S_0(x_s, y_s, z_s)$ is a point on a shrunken edge, and its projection on the approaching face β is $P_0(x_p, y_p, z_p)$, which is the contact point. S_1 and P_0 represent the locations of S_0 and P_0 after displacement increments (u_s, v_s, w_s) and (u_p, v_p, w_p) , respectively. The normal displacement Δd_n of the contact can be determined from

$$\Delta d_n = \mathbf{n}_\beta \cdot \mathbf{P}'_0 S_1 - \mathbf{n}_\beta \cdot \mathbf{P}_0 S_0 = \mathbf{n}_\beta \cdot \begin{bmatrix} x_s + u_s - x_p - u_p \\ y_s + v_s - y_p - v_p \\ z_s + w_s - z_p - w_p \end{bmatrix} - \mathbf{n}_\beta \cdot \begin{bmatrix} x_s - x_p \\ y_s - y_p \\ z_s - z_p \end{bmatrix} = \mathbf{n}_\beta \cdot \begin{bmatrix} u_s - u_p \\ v_s - v_p \\ w_s - w_p \end{bmatrix} \quad (16)$$

where \mathbf{n}_β is the unit normal vector of face β . The displacement increments of S_0 and P_0 can be written in the following forms:

$$\begin{Bmatrix} u_s \\ v_s \\ w_s \end{Bmatrix} = N_i(x_s, y_s, z_s) \mathbf{u}_i \quad (17)$$

$$\begin{Bmatrix} u_p \\ v_p \\ w_p \end{Bmatrix} = N_j(x_p, y_p, z_p) \mathbf{u}_j \quad (18)$$

where N_i and N_j are the shape functions of faces α and β , respectively. \mathbf{u}_i and \mathbf{u}_j are the displacement increment vectors of the vertices on faces α and β , respectively. Eq. (16) can then be written as

$$\Delta d_n = \mathbf{n}_\beta \cdot N_i(x_s, y_s, z_s) \mathbf{u}_i - \mathbf{n}_\beta \cdot N_j(x_p, y_p, z_p) \mathbf{u}_j \quad (19)$$

Using the penalty method, a mathematical spring with stiffness K_n is placed between points S_0 and P_0 in the contact normal direction. The normal force increment, taking compressive force as positive, is calculated as

$$\Delta F_c^n = -K_n \Delta d_n \quad (20)$$

The total normal force is updated as

$$F_c^n(\tau + \Delta\tau) = F_c^n(\tau) + \Delta F_c^n \quad (21)$$

4.2. Shear contact force

The point \mathbf{P}_1 in Fig. 14 is the projection of S_1 onto the approaching face after the application of the displacement increment. The shear displacement Δd_s of the contact can be determined from

$$\Delta d_s = |\mathbf{P}'_0 \mathbf{P}_1| = \sqrt{|\mathbf{P}'_0 \mathbf{S}_1|^2 - \Delta d_n^2} \quad (22)$$

A shear contact spring is activated when the shear force is less than the shear resistance of a discontinuity. A mathematical spring with stiffness K_s is placed between points S_0 and P_0 in the direction parallel to the contact face. The shear force vector increment is calculated as

$$\Delta F_{ci}^s = -K_s \Delta d_s \quad (23)$$

The total shear force vector is updated as

$$F_{ci}^s(\tau + \Delta\tau) = F_{ci}^s(\tau) + \Delta F_{ci}^s \quad (24)$$

4.3. Failure criterion for a contact

When the state of a contact is opening or sliding, the contact forces should be adjusted according to the contact constitutive

relations. In this algorithm, a Coulomb friction law with a limited tensile strength is used. If the normal force satisfies

$$-F_c^n(\tau + \Delta\tau) > \sigma_t A_c \quad (25)$$

then both the normal and shear forces are set to zero. In the above formula, σ_t is the contact tensile strength and A_c is the contact area. Otherwise, the maximum shear force is calculated as

$$F_{c\max}^s = F_c^n \tan \varphi + c A_c \quad (26)$$

where φ is the friction angle and c is the contact cohesion. If the absolute value of the shear force given by

$$F_{ci}^s(\tau + \Delta\tau) = \sqrt{F_{ci}^s(\tau + \Delta\tau) F_{ci}^s(\tau + \Delta\tau)} \quad (27)$$

is greater than the maximum shear force, i.e.,

$$F_{ci}^s(\tau + \Delta\tau) \geq F_{c\max}^s \quad (28)$$

then the shear force is reduced to the limiting value as follows:

$$F_{ci}^s(\tau + \Delta\tau) = F_{ci}^s(\tau + \Delta\tau) (F_{c\max}^s / F_c^n(\tau + \Delta\tau)) \quad (29)$$

4.4. Equivalent nodal forces

As previously mentioned, a 3D contact can be established at any position between a shrunken edge and its approaching face. However, the nodal forces are necessary for the deformable element calculation. Therefore, the equivalent nodal forces should be obtained after the contact forces are obtained.

Let

$$\mathbf{F}^e = \{\mathbf{F}_1^e, \mathbf{F}_2^e \dots \mathbf{F}_n^e\}^T \quad (30)$$

Define the nodal forces to be statically equivalent to the contact forces acting on the face (α or β). Each of the forces \mathbf{F}_i^e must contain the same number of components as the corresponding nodal displacement \mathbf{u}_i and be ordered appropriately in the corresponding directions. The nodal forces can then be calculated from

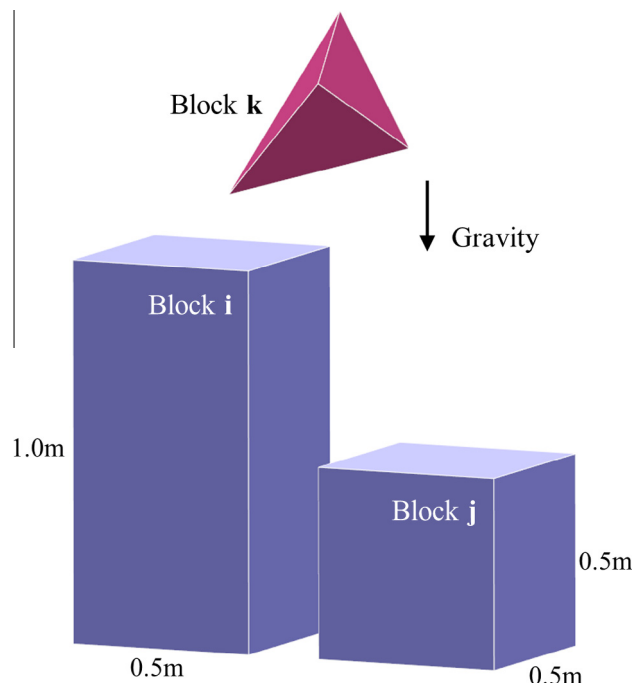


Fig. 17. Initial configuration of a three-block system.

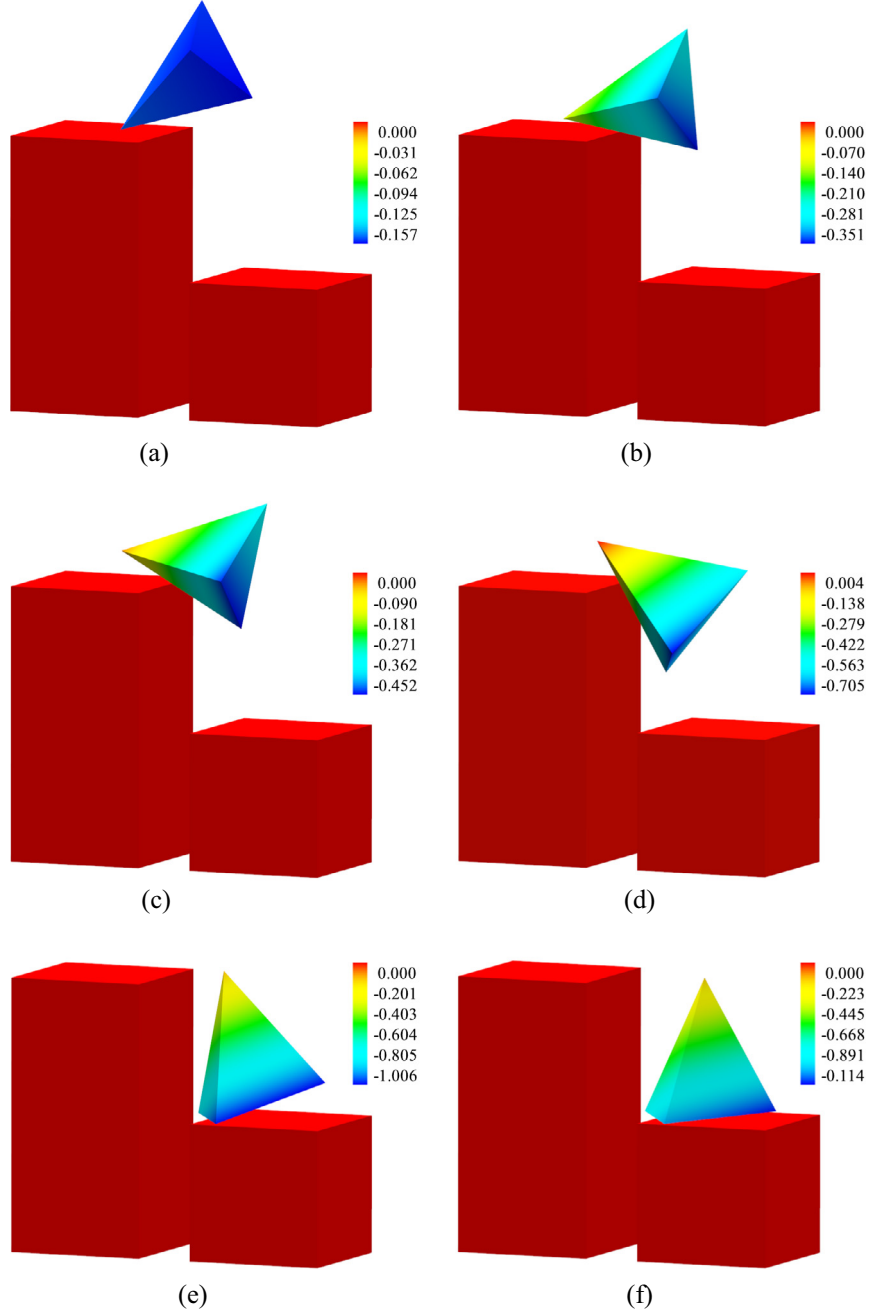


Fig. 18. The displacement in vertical direction of the three-block system after (a) 0.18 s, (b) 0.50 s, (c) 0.65 s, (d) 0.80 s, (e) 1.10 s and (f) 1.40 s (unit: m).

$$\mathbf{F}_i^e = \begin{Bmatrix} F_{ix}^e \\ F_{iy}^e \\ F_{iz}^e \end{Bmatrix} = \iint_{S_\sigma} N_i \mathbf{F}_c ds \quad (31)$$

where N_i is the shape function of the face and \mathbf{F}_c is the contact force vector in the corresponding direction.

5. Verification examples

The algorithm described in the previous sections was implemented in a VC++ program. Several examples are presented in the following sections to demonstrate the new contact detection algorithm.

5.1. Falling block

As shown in Fig. 15, the first case involves a system of two blocks. In this figure, the two blocks are triangular prisms. The bottom face of block **j** is fixed, and block **i** falls due to the gravitational force.

The values of the Young's modulus, Poisson's ratio and mass density for each block are $E = 35$ GPa, $\nu = 0.25$ and $\rho = 2700$ kg/m³, respectively. The stiffnesses of the normal contact spring and shear contact spring are 875 GN/m and 700 GN/m, respectively. The maximum time increment for each time step is 4×10^{-5} s. The initial velocity of block **i** is 0.0 m/s in the z direction.

The displacement in vertical direction of the block system based on the shrunken edge model is shown in Fig. 16, and the arrows in

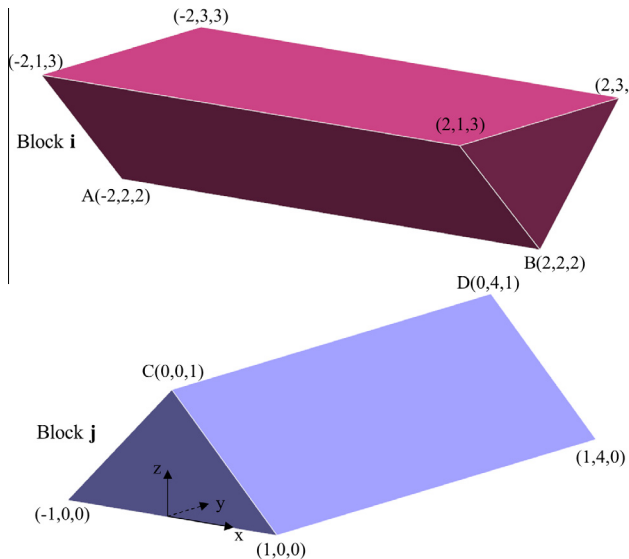


Fig. 19. Initial configuration of two prismatic blocks.

the figure indicate the behaviour of the top block. Block **i** falls and contacts block **j**, and contact between vertex B and vertex D is detected first (Fig. 16b). After the collision, the motion of block **i** is changed (Fig. 16c and d) due to the action of the contact forces. As the process continues, vertex-to-edge contact is detected between vertex A and edge CD, as shown in Fig. 16e. This case demonstrates that the shrunken edge model can accurately handle vertex-to-vertex and vertex-to-edge contacts.

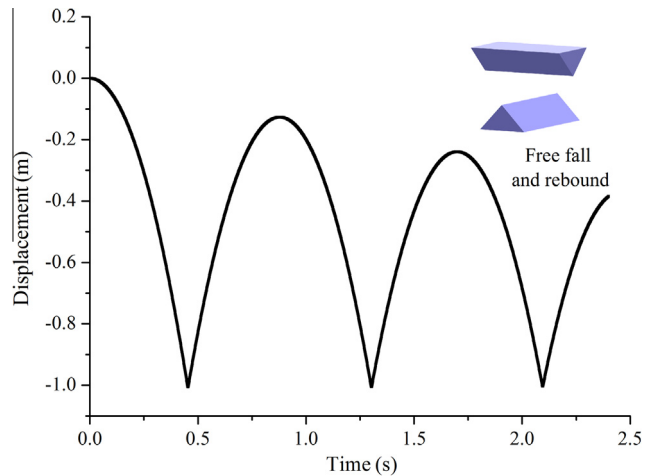


Fig. 21. Vertical displacement of block **i** during the free-fall and rebound motion.

Fig. 17 illustrates the geometry of a three-block system simulating the detection of vertex-to-face, edge-to-edge, edge-to-face and face-to-face contacts. Assume that the bottom faces of blocks **i** and **j** are fixed and that block **k** falls due to the gravitational force. The dimensions of block **i** are $0.5 \text{ m} \times 0.5 \text{ m} \times 1.0 \text{ m}$, and the dimensions of block **j** are $0.5 \text{ m} \times 0.5 \text{ m} \times 0.5 \text{ m}$. When block **k** contacts blocks **i** and **j**, the shrunken edge contact algorithm must model the contacts between the blocks.

The density, Young's modulus, Poisson's ratio and friction angle for each block are 2500 kg/m^3 , 30 GPa , 0.22 and 30° , respectively. The maximum time increment for each time step is $1 \times 10^{-5} \text{ s}$.

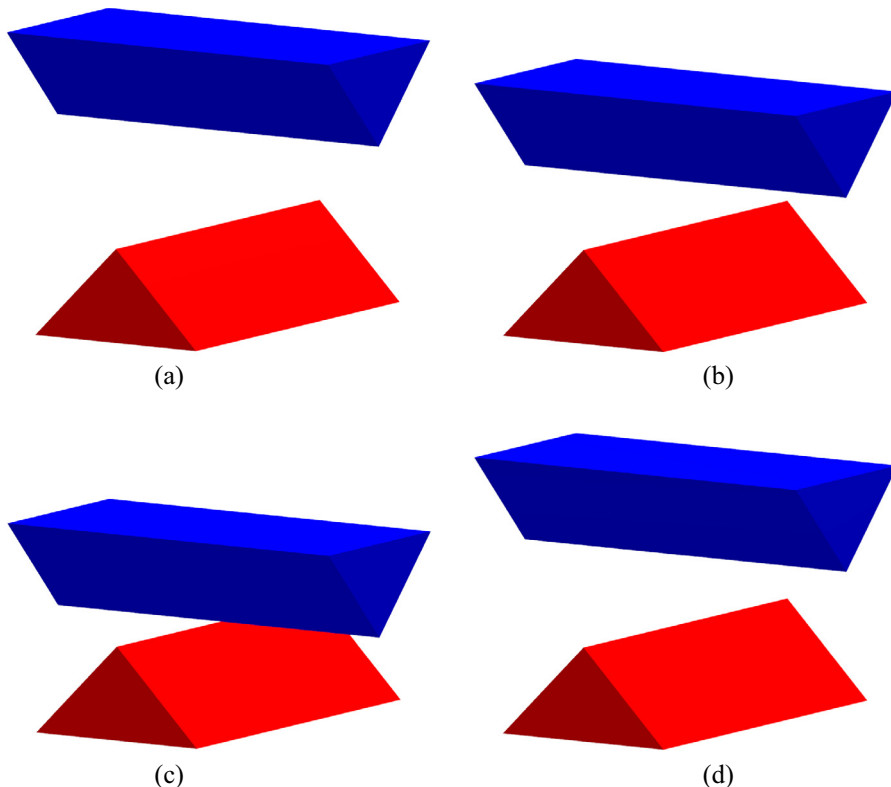


Fig. 20. Edge-to-edge contact after (a) 0.00 s, (b) 0.33 s, (c) 0.45 s and (d) 0.70 s.

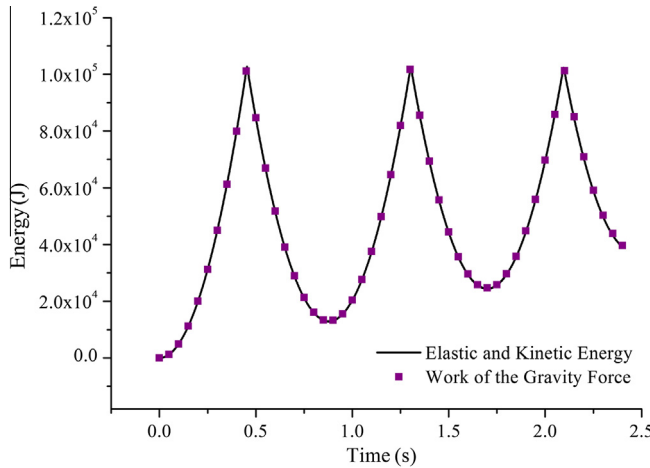


Fig. 22. Comparison of the work due to the gravitational force and the total elastic and kinetic energy.

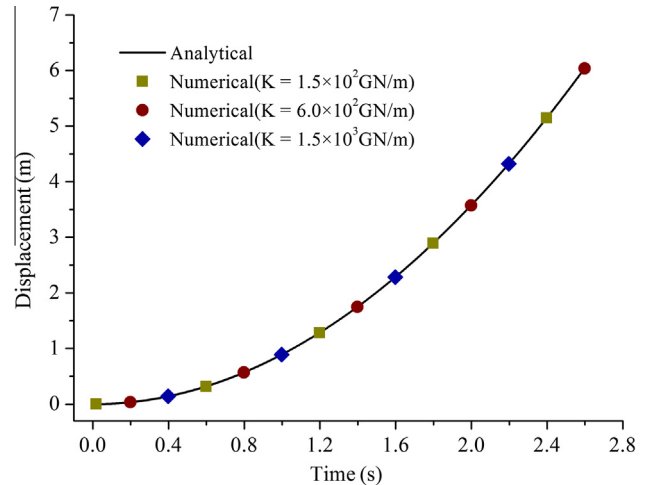


Fig. 25. Comparison of the analytical solution and numerical results using different penalty spring stiffnesses.

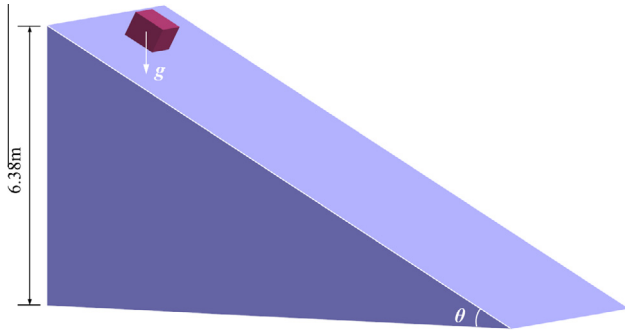


Fig. 23. A block sliding on an inclined plane.

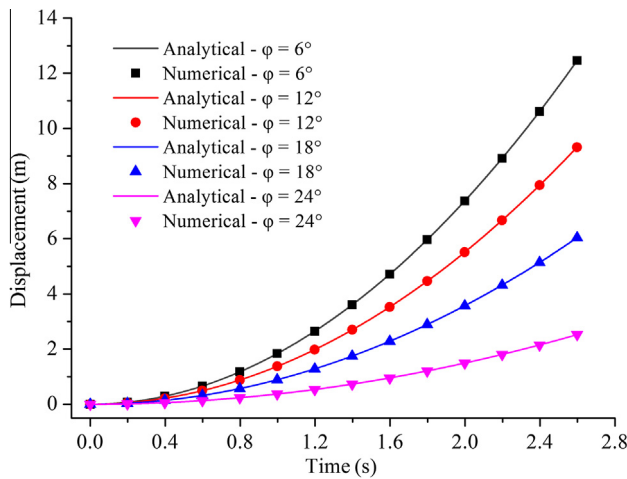


Fig. 24. Comparison of the analytical solution and numerical results.

The penalty spring stiffnesses in the normal and shear directions are 450 GN/m and 368 GN/m, respectively.

Fig. 18 shows the displacement in vertical direction of the three blocks during the interaction. No interpenetration occurs during the collision process. In this example, vertex-to-face (Fig. 18a), edge-to-edge (Fig. 18b-d), edge-to-face (Fig. 18e) and face-to-face

(Fig. 18f) contacts are verified, and the simulation results are reasonable.

5.2. Edge-to-edge contact between prismatic blocks

Fig. 19 illustrates the geometry of two prismatic blocks. This example is designed to simulate the detection of edge-to-edge contact between two blocks [31]. In this example, the bottom face of block **j** is fixed, and block **i** falls under the gravitational force. The values for the density, Young's modulus and Poisson's ratio of each block are $\rho = 2600 \text{ kg/m}^3$, $E = 2 \text{ GPa}$ and $\nu = 0.2$, respectively. The stiffness of the normal contact spring is 100 GN/m.

Fig. 20 shows the simulation results for this example using the shrunken edge algorithm. As shown in the figure, block **i** falls into contact with block **j**, and the edge-to-edge contact is detected (Fig. 20c). After the collision, block **i** rebounds due to the action of the contact forces. Due to the absence of damping in this example, the falling and rebounding motion repeats during the simulation. The resulting vertical displacement of block **i** is as shown in Fig. 21, which can be used to analyse the numerical results quantitatively. From the lowest positions in the displacement curve, we can conclude that no interpenetration occurs in the process. Additionally, the work performed by the gravitational force is compared with the total elastic and kinetic energy in Fig. 22, which demonstrates the conservation of energy in the calculation.

5.3. Block sliding on an inclined plane

It is important in numerical simulation to verify the results using simple geometries for which analytical solutions exist [36]. The example shown in Fig. 23 simulates the sliding of a block on an inclined plane at an angle θ to the horizontal.

When the friction angle φ is less than angle θ , the block will accelerate down the slope under the action of the gravitational force. The analytical solution for the displacement s at time t of the block starting from rest is

$$s(t) = \frac{1}{2}at^2 = \frac{1}{2}(g \sin \theta - g \cos \theta \tan \varphi)t^2 \quad (32)$$

where g is the gravitational acceleration. The inclination of the modelled plane is 28° , and the density, Young's modulus and Poisson's ratio of both blocks are 2500 kg/m^3 , 30 GPa and 0.22 , respectively. The stiffnesses of the normal and shear contact springs are 1500 GN/m and 1230 GN/m, respectively. Friction angles of 6° ,

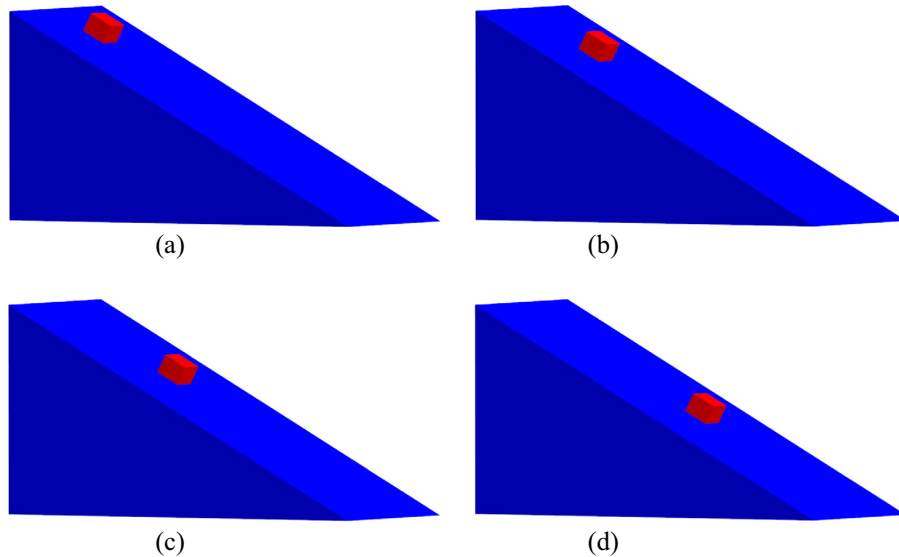


Fig. 26. The motion of the block after (a) 0.8 s, (b) 1.4 s, (c) 2.0 s and (d) 2.6 s.

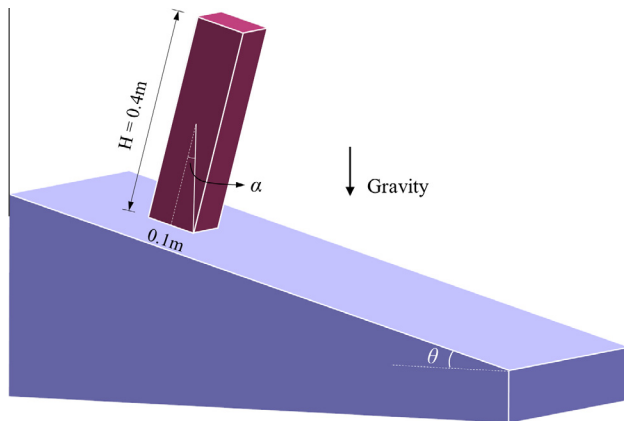


Fig. 27. A block toppling on an inclined plane.

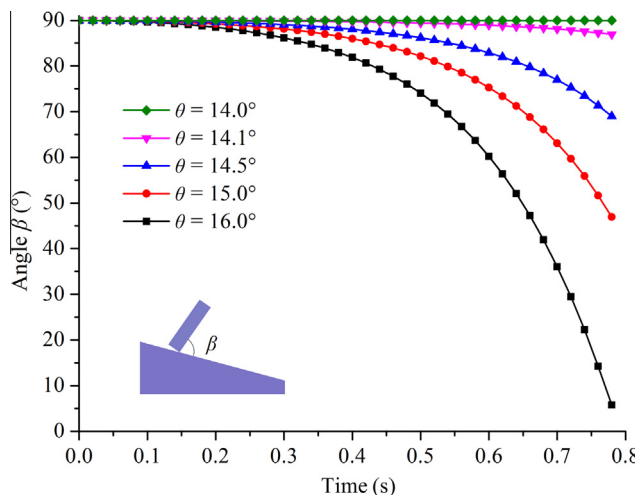


Fig. 28. Change in angle β during the toppling motion at different slope angles.

12° , 18° and 24° are investigated. The maximum time increment for each time step is 2×10^{-5} s, and the accumulated displacements are calculated up to 2.6 s.

In Fig. 24, the numerical results are compared with the time-dependent displacement predicted by the analytical solution in Eq. (32). The dots denote the numerical results, and the solid lines represent the corresponding analytical solution. The maximum relative error is less than 0.001% for all friction angles. The numerical results display satisfactory agreement with the analytical solutions.

The example is solved again with $\varphi = 18^\circ$. Comparisons between the analytical solution and numerical results using different penalty spring stiffnesses are shown in Fig. 25. The results show that the shrunken edge model is able to solve the sliding block problem well with different penalty values. The motion of the blocks for $K_n = 150$ GN/m after 0.8, 1.4, 2.0 and 2.6 s are shown in Fig. 26. No block interpenetration occurs even when the penalty is small.

5.4. Block toppling on an inclined plane

As shown in Fig. 27, for a block on an inclined plane, if the slope angle θ is less than the friction angle φ , then the block will remain still if rotation is not considered. However, if the slope angle θ is greater than the angle α , the block will begin to rotate [37]. The angle α can be calculated from the dimensions of the block, as expressed by

$$\alpha = \frac{180}{\pi} \times \arctan \left(\frac{W}{H} \right) \quad (33)$$

where W and H are the width and height of the block, respectively. In the figure, angle α equals 14° when W and H are 0.1 m and 0.4 m, respectively. We assume that the density is 2500 kg/m 3 , that the Young's modulus is 30 GPa and that the Poisson's ratio is 0.22 for each block. The stiffnesses of the normal and shear contact springs are 150 GN/m and 123 GN/m, respectively.

Slope angles θ of 14.0° , 14.1° , 14.5° and 16.0° are investigated. The numerical results for these cases are shown in Figs. 28 and 29. Let β denote the intersection angle between the block and the inclined plane. Fig. 28 shows angle β during the toppling motion. From this figure, the critical value for angle θ is 14.1° ,

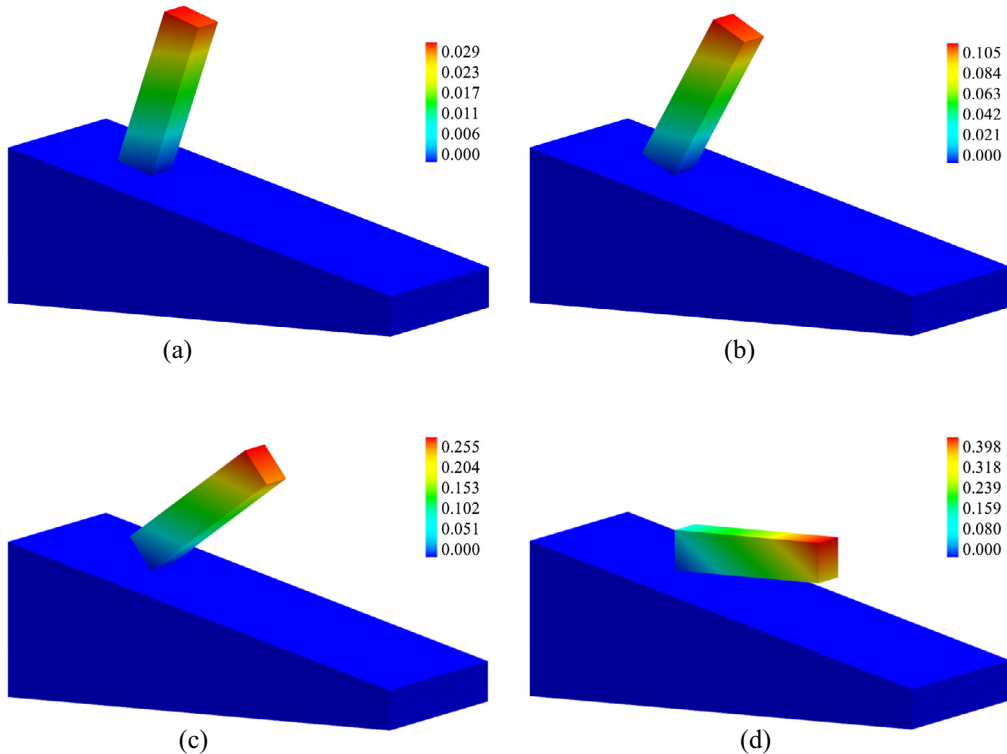


Fig. 29. The horizontal displacement of the block after (a) 0.40 s, (b) 0.60 s, (c) 0.76 s and (d) 0.88 s (unit: m).

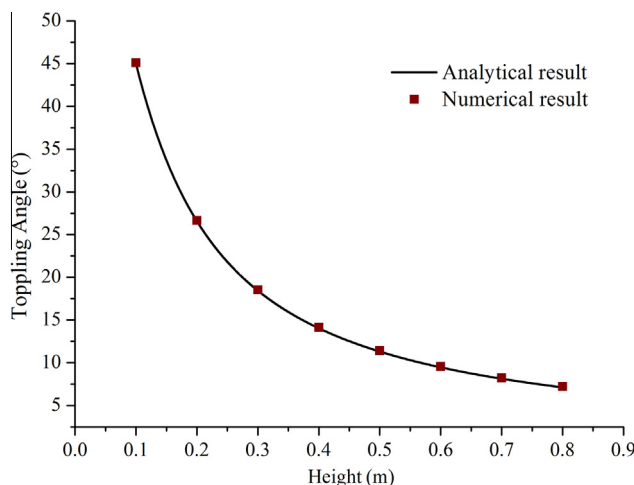


Fig. 30. Comparison of the critical toppling angle predicted by the numerical and analytical results for different block heights.

which corresponds well with the analytical solution. The horizontal displacement of the block after 0.4 s, 0.6 s, 0.8 s and 0.9 s for $\theta = 15.0^\circ$ is shown in Fig. 29. In the process, the modelling of face-to-face and edge-to-face contacts is verified.

In the above simulation, the height of the block is constant at 0.4 m. Based on Eq. (33), if the height is changed, the critical toppling angle will also change. A comparison of the critical toppling angle predicted by the analytical and numerical results for different block heights is shown in Fig. 30. The results show that the shrunken edge algorithm can successfully model toppling problems.

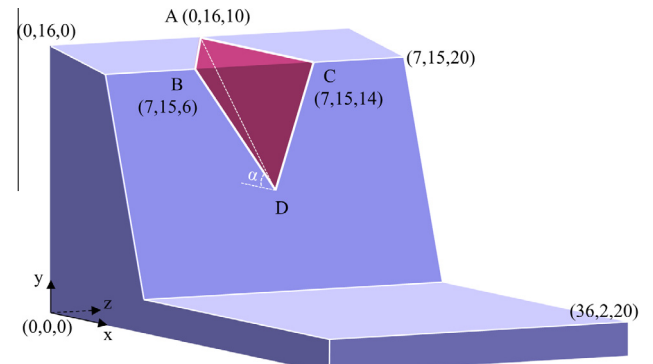


Fig. 31. Geometric model of a sliding tetrahedral wedge.

Table 1
Mechanical properties of the tetrahedral wedge.

Parameters	Value
Density ρ	2600 kg/m ³
Young's modulus E	20 GPa
Poisson's ratio ν	0.25
Normal spring stiffness K_n	200 GN/m
Shear spring stiffness K_s	160 GN/m

5.5. Wedge sliding and failure

Wedge sliding is one of the most common failure phenomena in rock slopes. A wedge is always created by a slope surface and the

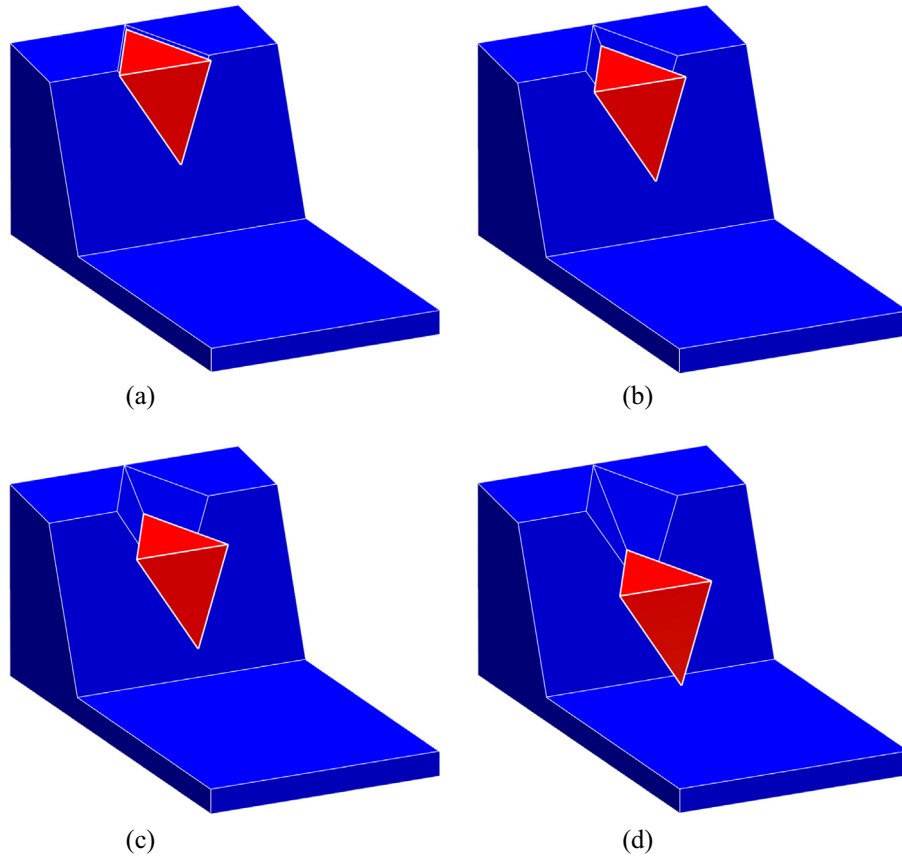


Fig. 33. The motion of the wedge after (a) 0.4 s, (b) 0.8 s, (c) 1.2 s and (d) 1.6 s.

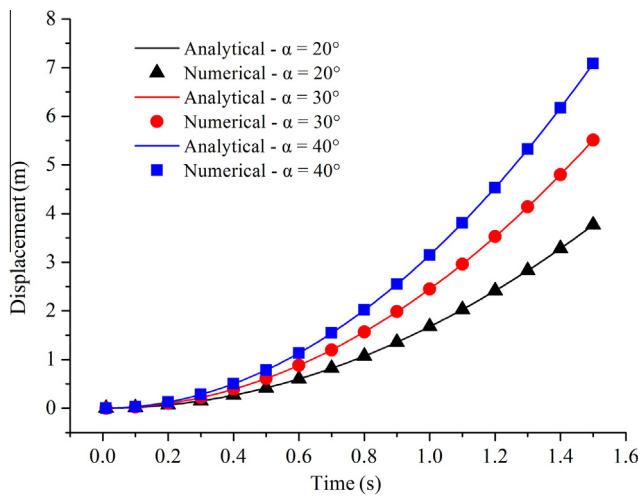


Fig. 32. Comparison of the analytical solution and numerical results for a tetrahedral sliding wedge.

intersection of two discontinuity planes [38]. The wedge tends to slide under gravitational force without sufficient frictional resistance. In this section, the sliding and failure process of a tetrahedral wedge is simulated to further test the new contact detection algorithm. Fig. 31 shows a symmetrical tetrahedral wedge ABCD sliding on two intersecting frictionless planes. AB is the line of intersection of the two planes, and α is the dip angle of AB. The

analytical solution for the displacement $s(t)$ at time t from the resting state is

$$s(t) = \frac{1}{2}gt^2 \sin \alpha \quad (34)$$

where g is the gravitational acceleration. Dip angles α of 20° , 30° and 40° are investigated. The position of point D changes with the angle α .

The mechanical properties of the tetrahedral wedge are listed in Table 1. The cohesion, tensile strength and friction angle of the intact rock are 8.6 MPa, 5.3 MPa and 30° , respectively. In both planes ABD and ACD, the friction angle and cohesion are set to 0. The maximum time increment for each time step is 1×10^{-5} s.

Fig. 32 shows the comparison of the analytical solution from Eq. (34) and the numerical results obtained using the shrunken edge model. The figure shows that the numerical results correspond well with the analytical solution for the tetrahedral sliding wedge model. Fig. 33 shows the motion of the sliding wedge for $\alpha = 40^\circ$. The purpose of this test is to verify that the numerically predicted failure mode is consistent with the analytical prediction. The contacts are detected on planes ABD and ACD throughout the wedge sliding process.

Finally, the tetrahedral wedge collides with the ground. Fig. 34 shows the failure of the wedge after the collision. In this example, the face-to-face, vertex-to-face and edge-to-edge contacts are verified, and no excessive interpenetration occurs.

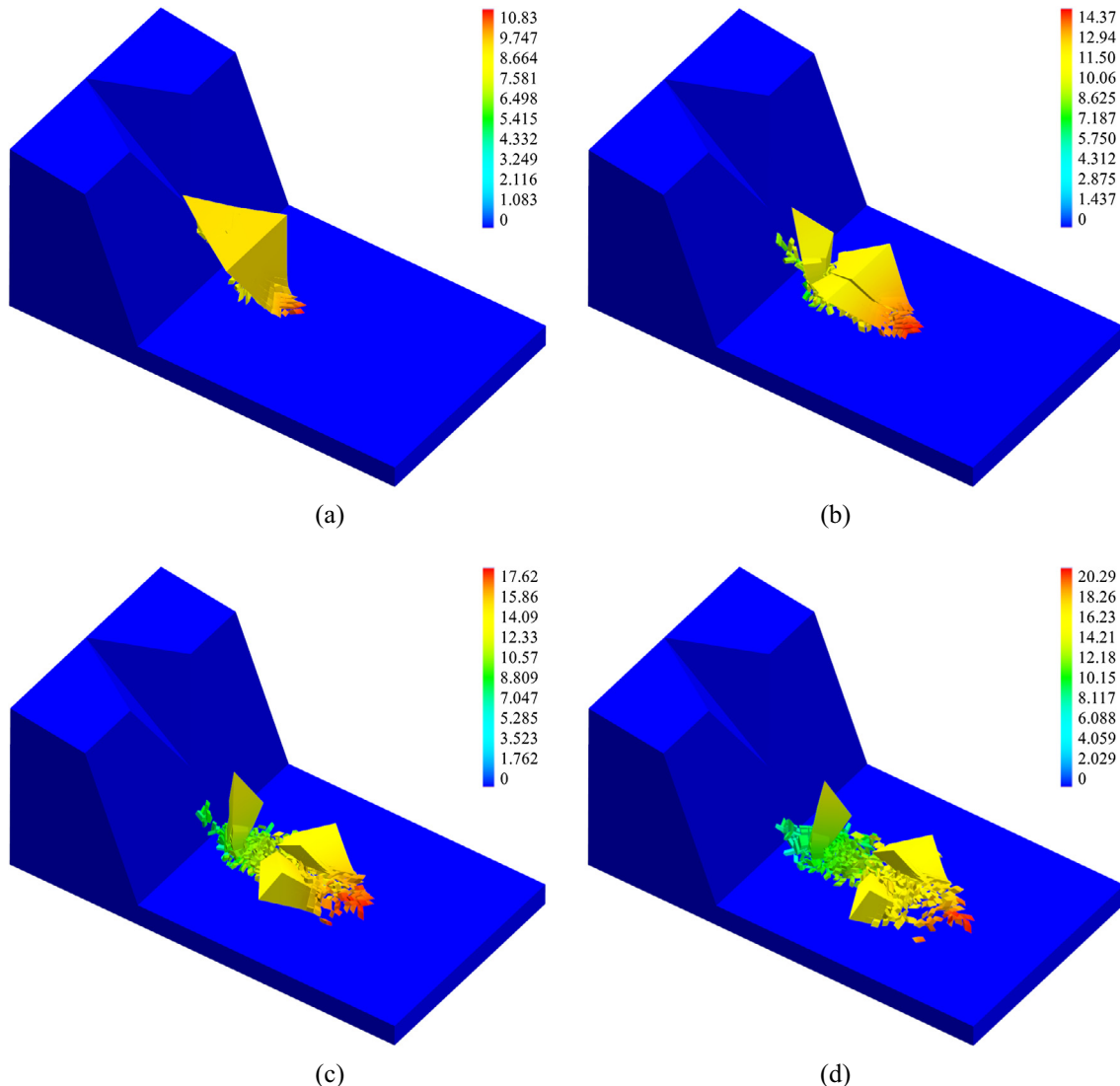


Fig. 34. The displacement in x -direction of the wedge after (a) 2.0 s, (b) 2.5 s, (c) 3.0 s and (d) 3.5 s (unit: m).

6. Conclusions

This paper shows how contact detection is performed between convex polyhedral blocks using the shrunken edge algorithm. In this algorithm, two contacting blocks are identified as a main block and a target block. The vertices of the main block are assumed to shrink toward the centre of the neighbouring faces. Shrunken edges are formed by these shrunken points. The procedure presented is an efficient and straightforward algorithm for the detection of all 3D contact types. The main advantages can be summarised as follows.

Compared to conventional search methods, this algorithm is unique in its use of shrunken edges. Using shrunken edges, it is easy to find the initial contact condition in a continuous block system and to model the transition from a continuum to a discrete condition, which are necessary steps in many hybrid continuous-discontinuous methods. Because the edges shrink into the neighbouring faces, geometric resolution can be performed between the main face and approaching faces, thus improving the efficiency of detection. To detect all six contact types in three dimensions, it is only necessary to distinguish the three possible geometric

relationships between the shrunken edge and the approaching face. The detection process is simple and efficient.

The accuracy and effectiveness of the new 3D contact algorithm are demonstrated through several examples involving two or more blocks that come into contact in a 3D domain. First, all six essential contact types are precisely detected in falling block examples. The algorithm is then validated by simulating several toppling and sliding problems and comparing the numerical results with the analytical predictions. The complete failure process of multiple interacting blocks is revealed dynamically. The test cases demonstrate that the new method can provide physically realistic simulation results involving large displacements and rotation.

This paper concentrates on establishing a contact searching algorithm which could be used to simultaneously simulate the fracture of continuous medium and the collision of discrete blocks. However, in some practical cases, it would be more appropriate to consider the aperture between blocks by changing vertices' coordinates, and thus changing the block volume slightly. Therefore, the combination of a model to describe aperture between blocks and shrunken edge model for contact detection between polyhedral blocks in a unified algorithm would be an interesting topic for further investigations.

Acknowledgements

The authors would like to acknowledge support from the National Basic Research Program of the Ministry of Science and Technology of China (Grant No. 2010CB731506), the National Key Technology Research and Development Program of the Ministry of Science and Technology of China (Grant No. 2012BAK10B01), the Strategic Priority Research Program (B) of Chinese Academy of Sciences (Grant No. XDB10030303) and the Youth Science Fund of the National Natural Science Foundation of China (Grant No. 11302230).

References

- [1] Jing L. A review of techniques, advances and outstanding issues in numerical modelling for rock mechanics and rock engineering. *Int J Rock Mech Min Sci* 2003;40(3):283–353.
- [2] Selvadurai APS, Yu Q. Mechanics of a discontinuity in a geomaterial. *Comput Geotech* 2005;32(2):92–106.
- [3] Ning YJ, An XM, Ma GW. Footwall slope stability analysis with the numerical manifold method. *Int J Rock Mech Min Sci* 2011;48(6):964–75.
- [4] Cheng YM. Advancements and improvement in discontinuous deformation analysis. *Comput Geotech* 1998;22(2):153–63.
- [5] Cundall PA. Formulation of a three-dimensional distinct element model—Part I. A scheme to detect and represent contacts in a system composed of many polyhedral blocks. *Int J Rock Mech Min Sci & Geomech Abstr* 1988;25(3):107–16.
- [6] Hart R, Cundall PA, Lemos J. Formulation of a three-dimensional distinct element model—Part II. Mechanical calculations for motion and interaction of a system composed of many polyhedral blocks. *Int J Rock Mech Min Sci Geomech Abstr* 1988;25(3):117–25.
- [7] Williams JR, O'Connor R. A linear complexity intersection algorithm for discrete element simulation of arbitrary geometries. *Eng Comput* 1995;12(2):185–201.
- [8] Shi GH. Discontinuous deformation analysis—a new numerical model for the statics and dynamics of block systems. PhD dissertation. UC Berkeley: Dept Civ Eng; 1988.
- [9] Wu JH, Ohnishi Y, Shi GH, et al. Theory of three-dimensional discontinuous deformation analysis and its application to a slope toppling at Amatoribashi, Japan. *Int J Geomech* 2005;5(3):179–95.
- [10] Ning Y, Yang J, An X, et al. Modelling rock fracturing and blast-induced rock mass failure via advanced discretisation within the discontinuous deformation analysis framework. *Comput Geotech* 2011;38(1):40–9.
- [11] Amir Reza Beyanaki S, Jafari A, Omid Reza Biabanaki S, et al. Nodal-based three-dimensional discontinuous deformation analysis (3-D DDA). *Comput Geotech* 2009;36(3):359–72.
- [12] Munjiza A, Owen DRJ, Bicanic N. A combined finite-discrete element method in transient dynamics of fracturing solids. *Eng Comput* 1995;12(2):145–74.
- [13] Munjiza A, Andrews KRF. Penalty function method for combined finite-discrete element systems comprising large number of separate bodies. *Int J Numer Meth Eng* 2000;49(11):1377–96.
- [14] Shi GH. Manifold method of material analysis. In: Proceedings of the trans ninth army conference on applied mathematics and computing, Minneapolis; 1991. p. 57–76.
- [15] Wu Z, Wong LNY. Frictional crack initiation and propagation analysis using the numerical manifold method. *Comput Geotech* 2012;39:38–53.
- [16] Jiang QH, Yeung MR. A model of point-to-face contact for three-dimensional discontinuous deformation analysis. *Rock Mech Rock Eng* 2004;37(2):95–116.
- [17] Keneti AR, Jafari A, Wu JH. A new algorithm to identify contact patterns between convex blocks for three-dimensional discontinuous deformation analysis. *Comput Geotech* 2008;35(5):746–59.
- [18] Liu XL, Lemos JV. Procedure for contact detection in discrete element analysis. *Adv Eng Software* 2001;32(5):409–15.
- [19] Zhi-Hua Z, Nilsson L. A contact searching algorithm for general contact problems. *Comput Struct* 1989;33(1):197–209.
- [20] Munjiza A, Andrews KRF. NBS contact detection algorithm for bodies of similar size. *Int J Numer Meth Eng* 1998;43(1):131–49.
- [21] Munjiza A. The combined finite-discrete element method. London: John Wiley & Sons; 2004.
- [22] Perkins E, Williams JR. A fast contact detection algorithm insensitive to object size. *Eng Comput* 2001;18(1–2):48–61.
- [23] Cohen JD, Lin MC, Manocha D, Ponamgi MK. I-collide: an interactive and exact collision detection system for large-scaled environments. In: Proceedings of the ACM symposium on interactive 3-D graphics (Monterey, CA, April 9–12); 1995. p. 189–96.
- [24] Itasca Consulting Group Inc. 3DEC-3D distinct element code. Minneapolis, USA: Itasca Consulting Group Inc; 1987.
- [25] Nezami EG, Hashash Y, Zhao D, et al. A fast contact detection algorithm for 3-D discrete element method. *Comput Geotech* 2004;31(7):575–87.
- [26] Nezami EG, Hashash YMA, Zhao D, et al. Shortest link method for contact detection in discrete element method. *Int J Numer Anal Meth Geomech* 2006;30:783–801.
- [27] Lin MC. Efficient collision detection for animation and robotics. PhD thesis. Berkeley: Department of Electrical Engineering and Computer Science, University of California; 1993.
- [28] Mirtich BV. Impulse based dynamic simulation of rigid body systems. PhD thesis. Berkeley: Department of Electrical Engineering and Computer Science, University of California; 1996.
- [29] Wu JH, Juang CH, Lin HM. Vertex-to-face contact searching algorithm for three-dimensional frictionless contact problems. *Int J Numer Meth Eng* 2005;63(6):876–97.
- [30] Yeung MR, Jiang QH, Sun N. Validation of block theory and three dimensional discontinuous deformation analysis as wedge stability analysis methods. *Int J Rock Mech Min Sci* 2003;40(2):265–75.
- [31] Wu JH. New edge-to-edge contact calculating algorithm in three-dimensional discrete numerical analysis. *Adv Eng Software* 2008;39(1):15–24.
- [32] Yeung MR, Jiang QH, Sun N. A model of edge-to-edge contact for three-dimensional discontinuous deformation analysis. *Comput Geotech* 2007;34(3):175–86.
- [33] Beyanaki S, Mikola RG, Hatami K. Three-dimensional discontinuous deformation analysis (3-D DDA) using a new contact resolution algorithm. *Comput Geotech* 2008;35(3):346–56.
- [34] Boon CW, Housby GT, Utili S. A new algorithm for contact detection between convex polygonal and polyhedral particles in the discrete element method. *Comput Geotech* 2012;44:73–82.
- [35] Feng C, Li S, Liu X, et al. A semi-spring and semi-edge combined contact model in CDEM and its application to analysis of Jiweishan landslide. *J Rock Mech Geotech Eng* 2013;6(1):26–35.
- [36] Beyanaki S, Ferdosi B, Mohammadi S. Validation of dynamic block displacement analysis and modification of edge-to-edge contact constraints in 3-D DDA. *Int J Rock Mech Min Sci* 2009;46(7):1223–34.
- [37] Chen G, Zheng L, Zhang Y, et al. Numerical simulation in rockfall analysis: a close comparison of 2-D and 3-D DDA. *Rock Mech Rock Eng* 2013;46(3):527–41.
- [38] He L, An XM, Ma GW, et al. Development of three-dimensional numerical manifold method for jointed rock slope stability analysis. *Int J Rock Mech Min Sci* 2013;64:22–35.